Structural and Dynamic Heterogeneity in Associative Networks Formed by Artificially Engineered Protein Polymers

Ameya Rao[1] *and Bradley D. Olsen*[1*]

[1]Department of Chemical Engineering, Massachusetts Institute of Technology, Cambridge, MA 02139

*Corresponding Author
Bradley D. Olsen
Tel: (617) 715-4548
Email: bdolsen@mit.edu

ABSTRACT: This work investigates static gel structure and cooperative multi-chain motion in associative networks using a well-defined model system composed of artificial coiled-coil proteins. The combination of small-angle and ultra-small-angle neutron scattering provides evidence for three static length scales irrespective of protein gel design which are attributed to correlations arising from the blob length, inter-junction spacing, and multi-chain density fluctuations. Self-diffusion measurements using forced Rayleigh scattering demonstrate an apparent superdiffusive regime in all gels studied, reflecting a transition between distinct "slow" and "fast" diffusive species. The interconversion between the two diffusive modes occurs on a length scale on the order of the largest correlation length observed by neutron scattering, suggesting a possible caging effect. Comparison of the self-diffusive behavior with characteristic molecular length scales and the single-sticker dissociation time inferred from tracer diffusion measurements supports the primarily single-chain mechanisms of self-diffusion as previously conceptualized. The step size of the slow mode is comparable to the root-mean-square length of the midblock strands, consistent with a single-chain walking mode rather than collective motion of multi-chain aggregates. The transition to the fast mode occurs on a timescale 10-1000 times the single-sticker dissociation time, which is consistent with the onset of single-molecule hopping. Finally, the terminal diffusivity depends exponentially on the number of stickers per chain, further suggesting that long-range diffusion occurs by molecular hopping rather than sticky Rouse motion of larger assemblies. Collectively, the results suggest that diffusion of multi-chain clusters is dominated by the single-chain pictures proposed in previous coarse-grained modeling.

INTRODUCTION

Associative polymer networks have attracted attention as functional soft materials due to their responsiveness, toughness, and self-healing abilities imparted by their dynamic bonds.[1–3] Because of their unique viscoelastic properties compared to covalently cross-linked networks, associative networks are promising for a variety of technologies, including biomedical hydrogels for tissue engineering and drug delivery[4,5] and artificial muscle and skin for soft robotics.[6,7] Their tunability for such applications stems from the diversity in their parameters for molecular design, including the chain architecture and concentration, number and spacing of stickers per chain, and association/dissociation kinetics and thermodynamics.[8–11] Extensive studies have established a strong effect of these molecular-scale parameters on the macroscopic behavior of the network, such as its timescales of relaxation and self-healing.[10,12–14] However, establishing quantitative relationships between individual bond and chain dynamics and macroscopic network response remains challenging due to the broad hierarchy of relaxation processes on different length scales, including conformational rearrangement and long-range self-diffusion.[13,15–17]

Associative polymer dynamics are often conceptualized using single-chain approaches, where individual molecules interact with a mean-field representation of the gel whose properties are governed by the constituent chains in a self-consistent manner.[18–20] This approach has led to several classical theories of associative polymer dynamics, including transient network theory[21–23] and sticky Rouse and reptation theories,[18,24,25] which incorporate the presence of the bonds as additional sources of friction that slow chain dynamics. More recently, simulations of single associative molecules in a mean-field background have demonstrated a previously unstudied interplay between distinct single-chain modes,[26,27] including molecular "walking" and "hopping," which can give rise to apparent superdiffusive behavior observed experimentally.[15,17,28,29]

Although these theories have provided substantial insight into the molecular processes underlying network relaxation and self-diffusion, single-chain conceptualizations largely neglect the effect of multi-chain correlations and network heterogeneity on the dynamics. Polymer networks often contain inhomogeneities on various length scales,[30–32] including irregular junction distributions and strand lengths,[33,34] topological defects such as loops and dangling ends,[35,36] and density variations caused by micro-phase-separated clusters.[34,37] In covalently cross-linked gels, these inhomogeneities are widely attributed to a kinetic trapping of the network structure due to the permanent junctions.[30,31] Similar static inhomogeneities have also been observed in reversible gels,[15,38–40] though they are unlikely to arise from the same kinetic trapping mechanism due to the ability to relax large-scale density variations by bond exchange.[17]

Static inhomogeneities reflecting multi-chain effects in associative networks have been shown to influence viscoelastic relaxation, particularly by delaying the onset of the terminal regime to lower frequencies.[41] However, the effect of structural features on self-diffusion of the network-forming molecules is still unclear, particularly as they relate to transitions between diffusive modes on length scales larger than the mesh size.[15,17,27] In addition, single-chain conceptualizations of diffusive mechanisms such as molecular walking and hopping cannot capture effects (if any) of inter-chain correlations on network dynamics, such as diffusion of multi-chain clusters.[18,42] Multi-chain motion has been suggested to underlie relaxation in associative networks under shear,[43,44] though its role in quiescent-state dynamics remains unclear. Notably, recent attempts to fit single-chain simulations of associative star polymers to experimental data have resulted in molecular sizes and relaxation times an order of magnitude too large,[26] possibly implying terminal diffusion by multi-chain aggregates rather than single molecules.

This work presents an experimental investigation into the role of static heterogeneity and multi-chain correlations on self-diffusion in a class of model associative networks with controllable molecular architecture. The associative networks are formed by artificial proteins with a multi-block architecture consisting of associative α-helical domains (also referred to as "coiled-coil" domains) flanked by flexible linker strands.[44–46] These proteins form a well-defined model system free of common sources of molecular heterogeneity such as chain dispersity and irregular sticker spacing seen in conventional polymer networks.[31,47] Despite their molecular monodispersity, structural characterization using small-angle and ultra-small-angle neutron scattering reveals a correlation length larger than the inter-junction spacing in gels of all chain architectures and concentrations, attributed to mild inhomogeneity in the junction spatial distribution. Self-diffusion measurements using forced Rayleigh scattering demonstrate a transition between "slow" and "fast" diffusive modes on a length scale comparable the large-scale inhomogeneity. In addition, the relevant length and time scales governing each self-diffusion mode are consistent with a transition from single-chain walking to hopping via release of all of a chain's stickers, as inferred from comparison to the single-sticker dissociation time obtained from diffusion of a single coiled-coil domain. Collectively, the results suggest that network heterogeneity and multi-chain effects play only a minor role in associative polymer self-diffusion on length scales larger than the inter-junction spacing, supporting the single-chain conceptualization in previous coarse-grained models.

EXPERIMENTAL METHODS

Protein hydrogel synthesis. D_2O (99.9% D) was purchased from Cambridge Isotope Laboratories. Maleimide-functionalized Alexa-Fluor 488 was purchased from Fluoroprobes. All other materials were purchased from Sigma Aldrich or VWR. All materials were used as received.

Protein synthesis and purification. The model associative proteins $PC_{10}P$, $PC_{30}P$, and $C_{10}(PC_{10})_4$ are formed by a multi-block architecture consisting of coiled-coil domains ("P") separated by flexible midblocks ("C_x") (see **Figure 1**). Variants of each protein containing a single cysteine residue, termed PC_5-cys-C_5P, PC_5-cys-C_{25}-P, and $C_{10}(PC_{10})_4$-cys, were also synthesized to enable site-specific labeling with a photochromic dye for self-diffusion measurements using forced Rayleigh scattering or a fluorophore for fluorescence microscopy studies. Finally, a single-sticker analog with the molecular architecture C_5PC_5-cys was synthesized for tracer diffusion measurements through each protein matrix. The encoding genes and amino acid sequences for $PC_{10}P$, $PC_{30}P$, $C_{10}(PC_{10})_4$, $C_{10}(PC_{10})_4$-cys, and C_5PC_5-cys, all in the pQE9 vector, have been previously reported.[37,44] Genes for PC_5-cys-C_5P and PC_5-cys-C_{25}-P were purchased from Genscript in the pUC18 vector and cloned into the pQE9 vector between the BamHI and HindIII restriction sites using standard molecular cloning protocols. The amino acid sequence for each protein is provided in the Supplementary Information (SI).

All genes were transformed into the SG13009 strain of *Escherichia coli*, which was streaked onto LB-agar plates supplemented with ampicillin and kanamycin and grown at 37 °C overnight. For each protein, a single colony was used to seed a 50 mL LB starter culture, which was used to inoculate 5 L of TB media supplemented with 200 mg/L ampicillin and 50 mg/L kanamycin. Cells were grown at 37 °C until the OD_{600} reached 0.8 – 1.0 and then induced with 1 mM of isopropyl β-D-1-thiogalactopyranoside. After 6 hours of protein expression, cells were harvested by centrifugation, resuspended in a denaturing buffer (8 M urea, 100 mM sodium phosphate, 10 mM tris, pH = 8.0), lysed by sonication, and clarified by centrifugation. Clarified lysates were purified by a combination of Ni^{2+}-NTA affinity chromatography, ammonium sulfate precipitation, and anion exchange chromatography using 2 5-mL HP-Q HiTrap (GE Healthcare) columns in series on an automated AKTA fast protein liquid chromatography system (GE Healthcare).

Site-specific labeling of cysteine-functionalized proteins. Cysteine-functionalized proteins were site-specifically labeled with maleimide-functionalized *o*-nitrostilbene (ONS-M) or maleimide-functionalized Alexa-Fluor 488 (AF-488) by thiol-maleimide coupling. The photochromic ONS-M dye was synthesized following a published procedure without changes.[48] Dye conjugation was performed in a co-solvent blend of dimethylformamide and urea buffer (6 M urea, 10 mM sodium phosphate) in a 3:1 vol ratio. After each protein was fully dissolved at a concentration of 2.5 mg/mL, 50 equiv of tris(2-carboxyethyl)phosphine hydrochloride relative to the cysteine residue was added to reduce preformed disulfide bonds, and the pH was adjusted to 7.2 using a pH meter. Then, 10 equiv of ONS-M or AF-488 was added dropwise from a stock solution of 8 mg/mL in dimethylsulfoxide, and the mixture was deoxygenated by bubbling with nitrogen for 45 min. The mixture was then stirred under nitrogen at room temperature overnight in the dark.

Dye-labeled proteins were purified from unconjugated dye by spin filtration and Ni^{2+}-NTA affinity chromatography. First, the reaction mixture was washed with ethyl acetate 3x in a separatory funnel to remove the dimethylformamide. Next, the aqueous layer containing the desired protein was centrifuged to remove precipitated free dye and spun at 4000*g* in a centrifugal filter (EMD Millipore, MWCO 3kDa) for 1 h at 4°C. Fresh urea buffer was added, and the centrifugal filtration was performed 7 times until the flow-through was colorless. To fully remove free dye, the flow-through was then purified by Ni^{2+}-NTA affinity chromatography in denaturing conditions. The purified dye-labeled protein was dialyzed against Milli-Q water and lyophilized.

Formation of associative protein hydrogels. Protein hydrogels were formed by dissolving lyophilized proteins in 100 mM sodium phosphate buffer at pH = 7.6 at the desired concentration. Weight-per-volume concentrations were calculated assuming a protein density of 1.3 g/mL as in previous work.[17] For forced Rayleigh scattering measurements, 5 wt% of dye-labeled protein was included in the gel. For fluorescence microscopy studies, 0.3 wt% of dye-labeled protein was included in the gel. For neutron scattering experiments, gels were prepared in a deuterated buffer (100 mM sodium phosphate in D_2O, pD = 7.6). Gel samples were stored at 4 ℃ for 2 days until they formed macroscopically homogeneous, optically transparent hydrogels.

Small-angle and ultra-small-angle neutron scattering. Small-angle neutron scattering (SANS) and ultra-small-angle neutron scattering (USANS) measurements were performed at the Spallation Neutron Source at Oak Ridge National Laboratory. Samples were prepared by sandwiching the protein gels between two quartz windows with a 1 mm Ti spacer and sealed in a Ti demountable cell. Sealed samples were then annealed at 80 °C for 5 min to remove thermal history and allow bubbles to float to the top of the cell outside of the 10 mm beam aperture. Measurements were performed at 25 °C. Samples were allowed to equilibrate at the measurement temperature for 30 min before acquiring data.

SANS measurements were performed at the EQ-SANS beamline at ORNL (BL-6). Two instrument configurations were used to cover a q-range of 0.5 – 7.3 nm^{-1}. The low-q configuration had a sample-to-detector distance of 4 m and a wavelength of 10 Å, while the high-q configuration had sample-to-detector distance of 2.5 m and a wavelength of 2.5 Å. The EQ-SANS instrument uses a 1 x 1 m^2 ^{3}He-tube detector with a resolution of 5.5 x 4.3 mm to detect scattered neutrons. All data were collected using a 10 mm beam aperture size. Scattered intensities were azimuthally averaged to convert them into 1D scattering patterns, corrected for empty cell scattering and blocked beam background, and calibrated to an absolute scale using a Porasil silica standard. The data from the two configurations were stitched together after 1D data reduction by matching overlapping q-ranges using the *drtsans* software.[49] To perform background subtraction of the solvent and empty cell, the solvent scattering was measured separately and subtracted from the gel scattering, scaled by the solvent volume fraction calculated from the protein weight-per-volume concentration assuming a protein density of 1.3 g/mL.[17]

USANS measurements were performed on a time-of-flight triple-bounce Bonse-Hart small-angle scattering spectrometer at ORNL SNS (BL-1A).[50,51] Neutron wavelengths of 0.9, 1.8, and 3.6 Å were used to access a q-range of 0.001 to 0.03 nm^{-1}. The source-to-detector distance was 30 m. The USANS instrument uses an 8-pack, staggered 0.5-inch diameter ^{3}He detector.[50] All data were collected using a 10 mm beam aperture size. USANS intensities were corrected for empty cell scattering and blocked beam background and calibrated to an absolute scale using a Porasil silica standard. For each sample, the USANS and SANS data were combined and analyzed using a common structural model across the entire wavevector range.

Forced Rayleigh scattering. Forced Rayleigh scattering (FRS) measurements were performed as described previously.[15,17,48] Gels were prepared with ~5 wt% of ONS-labeled chains, sandwiched between two quartz discs in a brass or aluminum sample cell, and equilibrated at the measurement temperature for 1 h before measurement. Temperature was controlled by a recirculating chiller. In a typical measurement, a 100 mW single-longitudinal-mode laser with wavelength λ was split into two coherent beams, which were recombined to intersect in the sample at an internal angle θ_i (calculated from Snell's law, assuming a gel refractive index of $n = 1.34$). Upon irradiation by the two beams for 0.2 – 1.0 s, the dye-labeled chains were selectively photobleached to create a holographic grating with period

$$d = \frac{\lambda}{2n \sin(\theta_i/2)} \tag{1}$$

The decay of the grating amplitude due to diffusion was monitored by diffraction of a single beam at the same wavelength and angle, attenuated by 10^4. The intensity decay was fit to either a single stretched exponential or the sum of two stretched exponentials with different time constants

$$I(t) = \left[A \exp\left(-\left(\frac{t}{\tau}\right)^{\beta}\right)\right]^2 + B \tag{2a}$$

$$I(t) = \left[A_1 \exp\left(-\left(\frac{t}{\tau_1}\right)^{\beta_1}\right) + A_2 \exp\left(-\left(\frac{t}{\tau_2}\right)^{\beta_2}\right)\right]^2 + B \tag{2b}$$

where $\tau_1 < \tau_2$ are the time constants, A_1 and A_2 are amplitudes, β_1 and β_2 are stretching parameters, and B is the incoherent background. At each measurement angle, the average diffusion time scale was determined as the first moment of the longest mode

$$\langle \tau \rangle = \frac{\tau}{\beta} \Gamma\left(\frac{1}{\beta}\right) \tag{3}$$

where Γ is the Gamma function. For fits to the sum of two exponentials, τ_2 was used as the longest time constant.

Two laser wavelengths ($\lambda = 355$ nm and $\lambda = 488$ nm) were used in both co-propagating and counter-propagating geometries[52] to access a wide experimental range of $d/2\pi \approx 25$ nm $-$ 10 μm. Each angle was measured in triplicate on different spots on the sample, and the diffusion timescales at each angle were averaged to ensure good statistics. All measurements were performed at 35 °C to ensure that the diffusion timescales were within the experimentally accessible window for all gels, including both self-diffusion and single-sticker tracer diffusion.

Fluorescence microscopy. Fluorescence microscopy of $PC_{10}P$ was performed on a Zeiss 980 Airyscan inverted laser scanning confocal microscope using a 63x oil-immersion lens and illumination at 488 nm (Coherent). Gels were prepared with 0.3 wt% of dye-labeled chains included and sandwiched between two coverslips separated by double-sided sticky Scotch tape. Image processing was performed using Zen.

Shear rheology. Oscillatory shear rheology was performed on an Anton Paar MCR 301 rheometer using a cone and plate geometry (25 mm, 1°). Mineral oil was used to coat the sides of the geometry to prevent dehydration. Gels were held at 45 °C for 30 min to allow them to relax and equilibrated at the measurement temperature for 30 min before acquiring data. Storage and loss moduli were obtained over a frequency range of 0.01 rad/s to 100 rad/s using a strain of 2%, which is within the linear viscoelastic regime.[17,44] All measurements were performed at 35 °C to match self-diffusion measurements obtained by FRS.

RESULTS AND DISCUSSION

Evidence for static inhomogeneity in associative networks. The artificial coiled-coil proteins $PC_{10}P$, $PC_{30}P$, and $C_{10}(PC_{10})_4$ are constructed with a multi-block architecture, with 2 or 4 associative α-helical domains (P) connected by flexible linkers ("C_x," with $x = 10,\ 30$). Above a volume fraction of $\phi \approx 0.05$ in aqueous buffer, the proteins form viscoelastic hydrogels held together by physical association of the coiled-coil domains in pentameric bundles (**Figure 1**). The aggregation behavior of the P domains into pentameric bundles in aqueous buffer has been extensively characterized in prior studies,[37,45,53] which demonstrate that it occurs due to a combination of electrostatic and hydrophobic interactions and remains stable at temperatures up to ~60 °C, beyond which the coiled-coil domains denature. While the P domains self-assemble into rod-like helices, the C_x domains can be approximated as random coils,[54] which serve as elastic strands bridging the coiled-coil junctions. Notably, the artificial proteins are nominally free of any sources of molecular heterogeneity that are often found in conventional polymer gels,[30,31] as the proteins have perfect monodispersity, sequence-defined sticker positions and strand lengths, and a well-defined sticker functionality and binding strength.[42,44,46] All gels are optically clear and macroscopically homogeneous by fluorescence microscopy (**Figure 1**C,D), suggesting the absence of large-scale clustering or phase separation.

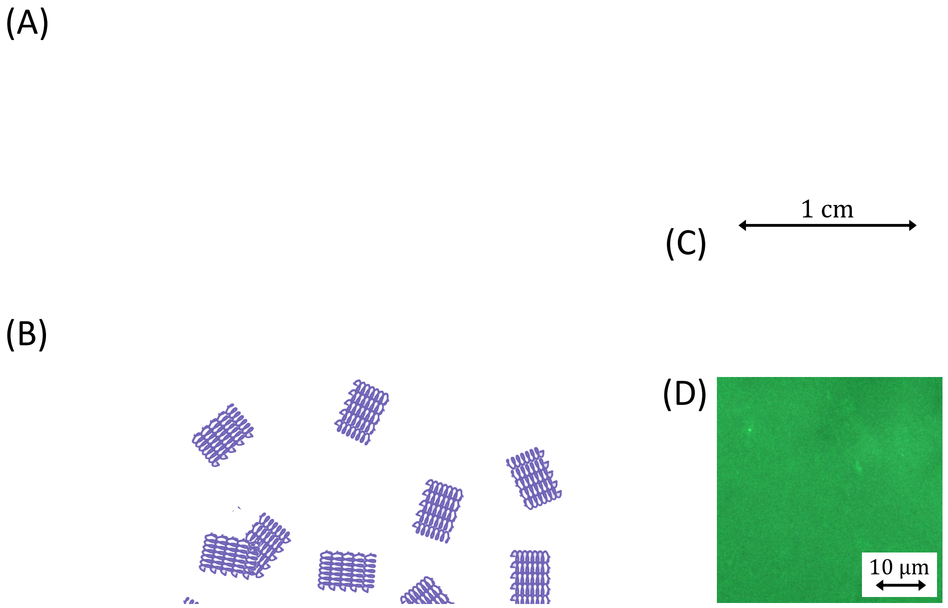

Figure 1. (A) Molecular structures and amino acid sequences of the three main artificial coiled-coil proteins used as model associative networks. (B) Schematic of the associative network formed by coiled-coil association in pentameric bundles. Three correlation length scales revealed by neutron scattering are illustrated. (C) Representative optical photograph of associative protein gel formed by $C_{10}(PC_{10})_4$ (10.5% w/v). (D) Representative fluorescence micrograph of associative

protein gel formed by $PC_{10}P$ (7% w/v), including 0.3 wt% of PC_5-cys-C_5P chains labeled with Alexa Fluor 488.

The static structure of the associative protein gels was characterized using a combination of small-angle neutron scattering (SANS) and ultra-small-angle neutron scattering (USANS) to access correlations across a wide range of length scales. Neutron scattering experiments were performed on gels prepared with hydrogenated proteins in a deuterated buffer to selectively probe the scattering from the protein network. Gel concentrations for each protein were chosen to match the coiled-coil junction concentration across different proteins (see Table S1). Neutron scattering patterns for each protein at various concentrations are shown in **Figure 2**, where both the SANS and USANS intensities were converted to absolute units using a porous silica standard.[51]

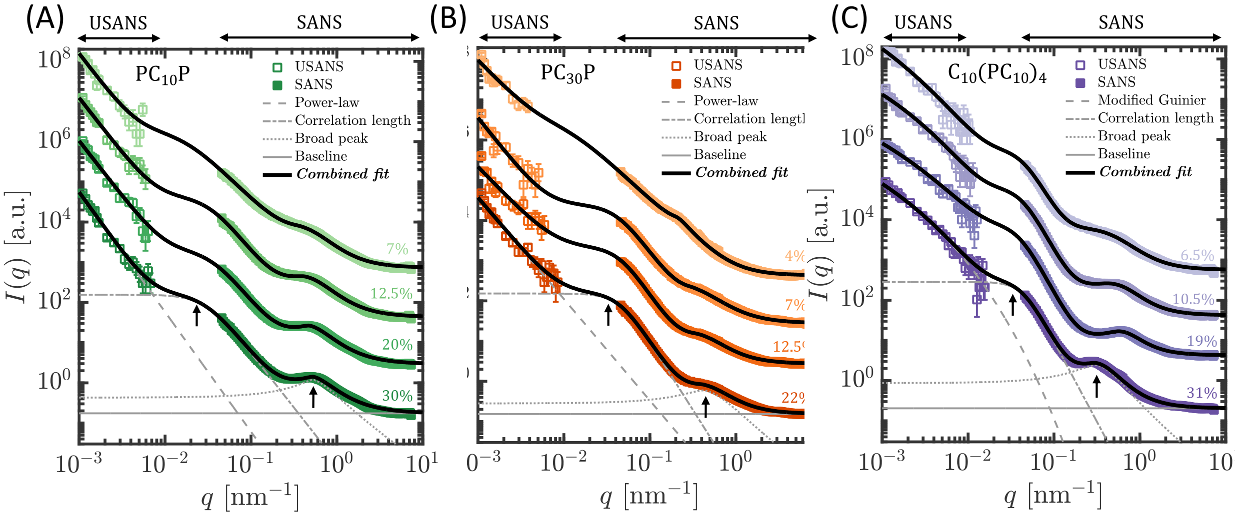

Figure 2. Combined small-angle and ultra-small-angle neutron scattering patterns for (A) $PC_{10}P$, (B) $PC_{30}P$, and (C) $C_{10}(PC_{10})_4$ gels of various concentrations. Curves are absolute intensities calibrated to a porous silica standard and are shifted vertically by 20x for clarity. Black lines indicate fits to the double-correlation-length model. For the bottom-most curves, the fit

components are shown in gray and the scattering features Ξ^{-1} and q_0 are indicated by the black arrows.

The combined neutron scattering patterns exhibit qualitatively similar features for all gels, including a monotonic decay in the low-q USANS region ($q < 0.02\ \mathrm{nm}^{-1}$), a power-law decay in the low-q SANS region ($0.04\ \mathrm{nm}^{-1} < q < 0.15\ \mathrm{nm}^{-1}$), a mid-$q$ peak or shoulder around $q \approx 0.4\ \mathrm{nm}^{-1}$, and a high-$q$ decay to the incoherent baseline. Although the q-ranges of the two techniques do not overlap, the curves are expected to reflect the same underlying gel structure. Both were calibrated into absolute units using the same porous silica standard.[51] Notably, a comparison of the relative intensities of the USANS and SANS regions suggests a plateau or peak in the intermediary region such that the two patterns connect smoothly; however, the exact nature of this scattering feature is unclear. It should be noted that this plateau could not be identified in previous structural studies of associative networks based on SANS alone,[15,38,55] demonstrating the importance of the USANS data in revealing this additional structural feature in the network.

To quantify relevant structural length scales, the combined scattering pattern for each gel was fit to a semi-empirical double-correlation-length model across the entire wavevector range, assuming that the total scattered intensity results from an additive contribution of the scattering from structural features on each length scale.[30,34,56]

$$I(q) = I_{large}(q) + I_{correlation\ length}(q) + I_{broad\ peak}(q) + I_{baseline} \tag{4}$$

Here, the first term captures the initial decay in the USANS region, the second term captures the scattering feature (i.e., plateau) in the intermediary region and the low-q power-law in the SANS region, the third term captures the mid-q peak or shoulder in the SANS region, and the fourth term captures the q-independent incoherent scattering from the protein network (note that the scattering from the deuterated buffer has been subtracted from the scattering patterns).

The specific functional form of each term was chosen to accurately reproduce the main features of the scattering patterns while minimizing the number of parameters required. For the telechelic $PC_{10}P$ and $PC_{30}P$ gels (panels A and B in **Figure 2**), the low-q region is well-captured by a simple power-law. However, for the multi-block $C_{10}(PC_{10})_4$ gels, a power-law does not have a sufficiently steep decay to allow fitting of the higher-q regions (see Figure S4), and for these gels a Guinier-like stretched exponential (which decays significantly faster with q) is used to capture the low-q scattering decay, similar to previous studies.[34,57,58] Thus, the first term in Eq. 4 is chosen as

$$I_{large}(q) = \begin{cases} \dfrac{A}{q^n}, & \mathrm{PC_xP\ gels} \\ A\exp\left(-R_{agg}^s q^s\right), & \mathrm{C_{10}(PC_{10})_4\ gels} \end{cases} \tag{5a}$$

where A is the component amplitude, n is a fractal dimension characterizing large-scale mass-fractal-like structures in the PC_xP gels, R_{agg} is a characteristic size of large-scale aggregates in the $C_{10}(PC_{10})_4$ gels, and s is a stretching parameter. The power-law upturn at low q seen for the telechelic PC_xP gels may indicate an additional large length scale (> 1 μm) also present in these gels, though it cannot be resolved as it is outside the USANS range. It should be noted that since the gels are optically clear and macroscopically homogeneous (see **Figure 1**C,D), scattering features on these large length scales may arise from artifacts such as dust and other impurities in the gel rather than the network structure itself; however, further study is required to identify their origin. The remaining terms in Eq. 4 describing correlations at larger wavevectors are identical for all proteins:

$$I_{correlation\ length}(q) = \frac{B}{1 + (\Xi q)^{m_1}} \tag{5b}$$

where Ξ is a large-scale correlation length that gives rise to the plateau in the intermediary region, B is the component amplitude, and m_1 is a fractal dimension characterizing the intermediate-scale mass-fractal-like network structure. Finally,

$$I_{broad\ peak}(q) = \frac{C}{1 + (|q - q_0|\xi)^{m_2}} \tag{5c}$$

where q_0 is a correlation peak or shoulder wavevector, ξ is the local blob screening length, C is the component amplitude, and m_2 is a high-q fractal dimension.

Fits to the double-correlation-length model (Eq. 4) accurately capture the combined scattering patterns for each gel, as seen in **Figure 2**. The fits reveal three key structural features in all gels (see Figure S2): the correlation blob size $\xi \sim 1$ nm, the correlation peak component $q_0^{-1} \sim 10$ nm, and the large-scale correlation length $\Xi \sim 30$ nm resulting from the plateau in the intermediary region between the SANS and USANS patterns. The peak component can be converted into a real-space domain size via $d_0 = 2\pi/q_0$. This length scale is assigned to the average distance between the coiled-coil junctions, as in previous studies,[15,55] where the scattering around this correlation peak is expected to be dominated by the coiled-coil bundles due to their large size. The assignment of this length scale to the inter-junction spacing is also qualitatively consistent with its concentration dependence, where a scaling of approximately the expected $d_0 \sim \rho_{junction}^{-1/3}$ is observed (Figure S2B). While the local blob size ξ is attributed to the fluctuation length scale of the overlapping C_x strands as in a semi-dilute solution,[59] the two larger length scales $2\pi/q_0$ and Ξ are likely to arise due to the physical cross-linking of the coiled-coil domains to create the space-spanning network; these scattering features may be suppressed in conditions where coiled-coil association is unfavored.[37,44,60]

The combination of USANS and SANS allows the largest correlation length, Ξ, to be quantified in the protein gels, in contrast to previous studies of associative networks based on SANS alone where only the power-law decay of the $I_{correlation\ length}(q)$ term could be identified within the accessible q-range.[15,37,38,55] The largest correlation length Ξ is $1-4$ times the inter-junction spacing $2\pi/q_0$, indicating heterogeneity in the junction and/or chain distribution within the network. The fractional root-mean-square static density fluctuation, $\langle\delta c^2\rangle^{\frac{1}{2}}/c$, associated with this correlation length can also be estimated from the scattering amplitude B in Eq. 5b, using the known relative scattering powers of the proteins and deuterated buffer as described in the SI.[30] From the best-fit values of B, the static density fluctuation associated with the length scale Ξ is found to range from 2% to 10% in the protein gels, depending on the total concentration (Figure S3).

In covalent polymer gels, static density inhomogeneities are widely seen on length scales of $10-100$ nm and attributed to kinetic trapping of the network topology due to the permanent cross-links.[30,31] Although similar inhomogeneities have been occasionally seen in physical gels,[39,40] they are likely to arise from a distinct mechanism than in covalent networks due to the ability for transient networks to relax large-scale concentration fluctuations by self-diffusion. In addition, previously studied associative gels were often based on non-specific interactions where the sticker spacing and junction functionality were not controlled,[39,40] which increased the likelihood for chain clustering and topological heterogeneity. In contrast, the protein gels here have a well-defined chain architecture and junction functionality with perfect monodispersity in the connecting strands. The presence of a large-scale correlation length in the associate protein gels here suggests that such inhomogeneity may be an inherent property of well-equilibrated polymer networks, even in the absence of molecular-level dispersity. Interestingly, the static density fluctuation in the protein gels, $\langle \delta c^2 \rangle^{\frac{1}{2}}/c$, appears to *increase* with junction density (Figure S3), which is contrary to the expected decrease in static heterogeneity at higher concentration in conventional polymer gels.[30,31] The static inhomogeneity in the protein gels here may be related to the variations in the local network topology (e.g., loops or dangling ends), which are expected to be present even in equilibrated networks[61] and may give rise to additional correlations in the junction density distribution. However, further study is required to elucidate the origins for the large-scale correlation length Ξ in the associative protein gels; this could potentially be achieved by deconvolution of static and dynamic inhomogeneities via light scattering[62,63] or neutron spin-echo spectroscopy.[33,64]

Self-diffusive length and time scales revealed by forced Rayleigh scattering. Self-diffusion of the coiled-coil proteins across a range of length scales was probed by forced Rayleigh scattering (FRS), as shown in **Figure 3**. FRS measurements were performed at 35 °C to ensure that diffusion timescales were within the experimentally accessible range ($\sim 10^{-2} - 10^{4}$ s) for gels of all concentrations and sticker densities. The self-diffusion measurements demonstrate an apparent superdiffusive regime on length scales of $d^2/4\pi^2 \approx 10^3 - 10^6$ nm^2 before transitioning to terminal Fickian diffusion on long length scales. These diffusive regimes are characterized by a phenomenological power-law relationship between the diffusion timescale $\langle \tau \rangle$ and the holographic grating spacing $d^2/4\pi^2$: $\langle \tau \rangle \sim (d^2/4\pi^2)^{\mu}$, where $\mu = 1$ is consistent with Fickian diffusion and $\mu < 1$ indicates apparent superdiffusive behavior. Qualitatively similar behavior has previously been seen in associative networks formed by different polymer architectures (star vs. linear), sticker chemistry (coiled-coil aggregation vs. metal-ligand coordination), sticker density (5 to 15 stickers per chain), and sticker spacing (statistically spaced along the backbone vs. clustered on the ends).[17,28,29,38] The results here expand the range of associative networks in which apparent superdiffusive behavior is observed to telechelic polymers containing only two stickers per chain.

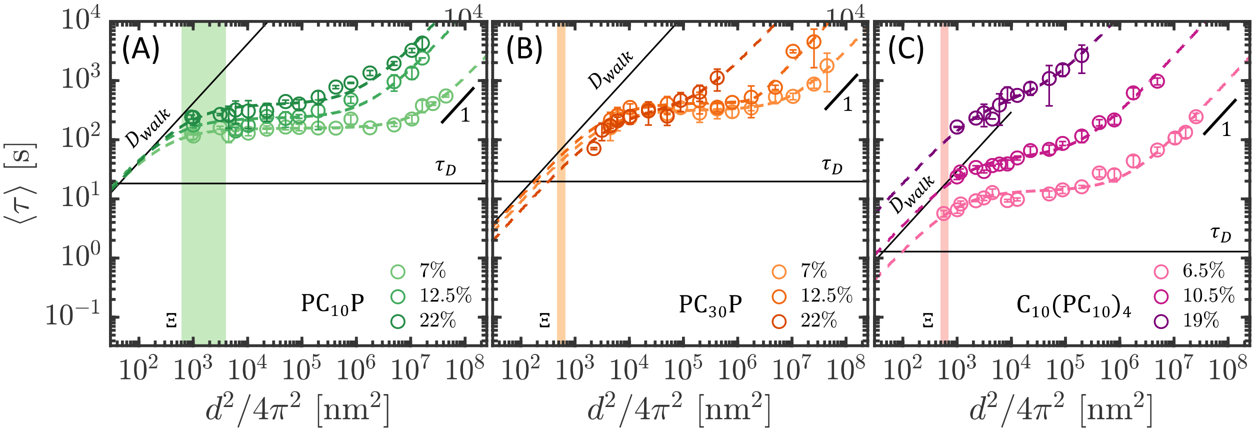

Figure 3. Self-diffusion measurements of (A) $PC_{10}P$, (B) $PC_{30}P$, and (C) $C_{10}(PC_{10})_4$ protein gels at various concentrations measured by forced Rayleigh scattering. Dashed lines are fits to the two-state model. Shaded regions show the range of the longest correlation length Ξ. Black solid lines show the single-sticker dissociation times τ_D inferred from tracer diffusion measurements and the single-molecule walking diffusivity estimated by $D_{walk} \approx R_{C_x}^2/\tau_D$.

Quantitative analysis of the two diffusive modes can be obtained by fitting the self-diffusion results to a previously developed two-state reaction-diffusion model,[17] which hypothesizes the presence of two distinct populations with diffusivities D_{slow} and D_{fast} and pseudo-first-order interconversion rates k_{on} and k_{off}. These four quantities are treated as adjustable parameters to fit each diffusion curve to the two-state model. A detailed discussion of the two-state model and its predicted diffusive regimes is provided in Refs.[16,17] and summarized in the SI. The two-state model demonstrates that the interconversion between the two diffusive populations over a finite length scale range gives rise to apparent superdiffusive scaling, and the width of the superdiffusive regime is proportional to the ratio of the two diffusivities weighted by their relative populations.[17,65] In single-chain models, the two diffusive modes are shown to be molecular walking and hopping.[26,27] However, the two-state model does not assign a molecular origin for each diffusive mode, leaving open alternative hypotheses such as collective cluster motion.[17] Further, it should be noted that the parameters k_{on} and k_{off} in the two-state model are not intended to represent physical rate constants (e.g., association and dissociation of a single coiled-coil sticker) but rather effective interconversion rates between the two apparent species. It should also be emphasized that the presence of distinct diffusive populations is a unique observation of the FRS measurement because it samples a moment of the spatial distribution that is sensitive to the presence of multiple populations, compared to the mean-square displacement which is sensitive only to the average of all populations and displays only Fickian scaling.[26]

The two-state model adequately captures the self-diffusive behavior over a large length scale range for all protein gels, as shown in **Figure 3**. The terminal diffusion coefficient, D_{eff}, can be calculated from the best-fit parameters as

$$D_{eff} = D_{fast}\left(\frac{\gamma\kappa_{eq}+1}{\kappa_{eq}+1}\right) \tag{6}$$

where $\gamma = D_{slow}/D_{fast}$ and $\kappa_{eq} = k_{on}/k_{off}$. Thus, the terminal self-diffusivity is proportional to the diffusivity of the fast mode weighted by its population.[17] As shown in Figure S10, the terminal diffusion coefficients for all protein gels decrease with concentration roughly consistent with the sticky Rouse prediction of $D_{eff} \sim \phi^{-5.19}$.[18] The four-sticker $C_{10}(PC_{10})_4$ gels display a noticeably stronger concentration dependence in their terminal diffusivity than the telechelic PC_xP gels, possibly due to differences in the number of stickers per chain. It should be noted that the sticky Rouse model may not strictly apply to the protein gels studied here, as it was formulated to describe chains with a large number of stickers along the backbone and a large degree of polymerization between stickers.[18]

From the two-state model parameters, characteristic length scales governing the transition between the two diffusive modes can be calculated:

$$\frac{d_{slow}}{2\pi} = \sqrt{\frac{D_{slow}}{k_{off}}} \qquad (7a)$$

and

$$\frac{d_{fast}}{2\pi} = \sqrt{\frac{D_{eff}}{k_{off}}} \qquad (7b)$$

Here, $d_{slow}/2\pi$ can be interpreted as a characteristic length scale up to which molecules undergo diffusion via the slow mode before transitioning to the fast mode, which determines the onset of the superdiffusive regime. In contrast, $d_{fast}/2\pi$ is the characteristic length of a single diffusive "step" in the fast mode, which determines the onset of terminal Fickian diffusion on long length scales. It should be noted that Equations 7a and 7b indicate the central role of the interconversion rate k_{off} in governing the length scale of each diffusive mode.

A comparison of the dynamic length scales $d_{slow}/2\pi$ and $d_{fast}/2\pi$ as a function of volume fraction for all protein gels is presented in **Figure 4**A, along with the static length scales ξ, $2\pi/q_0$, and Ξ from neutron scattering. The dynamic length scales for the slow mode are within the range $d_{slow}/2\pi = 20 - 70$ nm and approximately constant with concentration for each protein, consistent with a dissociation-controlled process for the transition to the fast mode. In contrast, the step size for the fast mode is on the order of $d_{fast}/2\pi \approx 10^2 - 10^4$ nm and noticeably decreases with concentration, suggesting an association-controlled process. In the single-chain view, these length scales are expected to be related to the mean-square displacement of molecules (1) by walking before complete dissociation and (2) for a single hopping step before reattaching to the network, respectively.[27] The results here are consistent with these single-chain mechanisms, though the single-molecule hopping displacements inferred from $d_{fast}/2\pi \approx 1$ μm may be unrealistically large for free diffusion of single molecules before reattachment. The concentration dependence of d_{fast} displays a scaling close to $\sim\phi^{-2}$ for all proteins, which is stronger than that expected for a simple linear scaling of the free binding site density with concentration (which would result in $d_{fast}\sim\phi^{-1/2}$). This may arise from a nonlinear dependence of the free site density with total concentration or a reduction in D_{fast} due to the higher local viscosity at higher concentration.[15,66] The strong concentration dependence in the hopping distance is also seen for single-sticker tracers through the same protein gels (Figure S11), further suggesting a reduction in the free chain diffusivity with concentration such that released chains cannot diffuse as far before reattaching to the network.

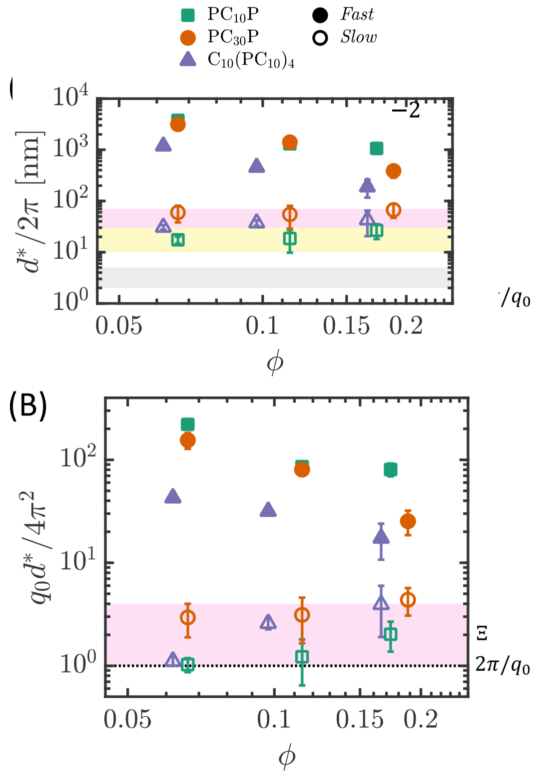

Figure 4. (A) Transition length scales $d_{slow}/2\pi$ and $d_{fast}/2\pi$ as a function of volume fraction for all proteins gels. (B) Transition length scales non-dimensionalized by the inter-junction spacing, $2\pi/q_0$, obtained from neutron scattering. For both panels, shaded regions indicate the range of the static length scales ξ, $2\pi/q_0$, and Ξ obtained from neutron scattering.

Previous studies have suggested the importance of the inter-junction spacing in establishing a fundamental mesh size that renormalizes network dynamics on longer length scales.[28,38,67] To examine the effect of the mesh size on the characteristic diffusive length scales, **Figure 4**B plots the length scales of the slow and fast diffusive modes normalized by the protein gels' inter-junction spacing, $2\pi/q_0$. As shown by this non-dimensionalization, the slow mode for all gels persists for only $1-4$ times the inter-junction spacing before chains transition to the fast mode, demonstrating the minimal contribution of the slow mode to diffusion on long length scales. In addition, a significantly stronger concentration dependence is seen in the normalized slow mode length scale for the multi-block $C_{10}(PC_{10})_4$ gels compared to the telechelic PC_xP gels, consistent with the reduced likelihood of disengagement of chains with more stickers at higher concentration. Interestingly, the length scale for the slow mode is on the order of the static inhomogeneity length scale Ξ seen in neutron scattering. This similarity may reflect a caging effect induced by the static density fluctuation associated with this large-scale correlation length in governing the transition between the slow and fast self-diffusive modes. In particular, the transition timescale k_{off}^{-1} may be related to the characteristic lifetime of multi-chain density fluctuations as the network dynamically reconfigures its topology, enabling the fast mode to take effect beyond this timescale.

Connecting self-diffusion timescales to single-sticker dynamics. Further insight into the molecular underpinnings of the self-diffusive modes in the protein gels can be obtained by connecting characteristic self-diffusion length and time scales with dynamics of the individual coiled-coil domains. Single-sticker bond lifetimes were inferred from FRS measurements of single coiled-coil domains through the $PC_{10}P$, $PC_{30}P$, and $C_{10}(PC_{10})_4$ gel matrices of the same concentrations (see **Figure 5**A), as previously done for small-molecule stickers in metal-coordinate gels.[16] The single-sticker tracer was designed with a single coiled-coil P domain flanked by C_5 domains on either side, resulting in the molecular structure C_5PC_5. This ensures that the local structure of the coiled-coil domain in the tracer to resemble the coiled-coil domains forming the network junctions while approximating the steric effects of the flanking C_x strands. Gel samples were prepared with 5 wt% of ONS-labeled C_5PC_5 tracers dispersed into the unlabeled gel matrix; with this low concentration it could be assumed that interaction between the C_5PC_5 tracers was negligible.

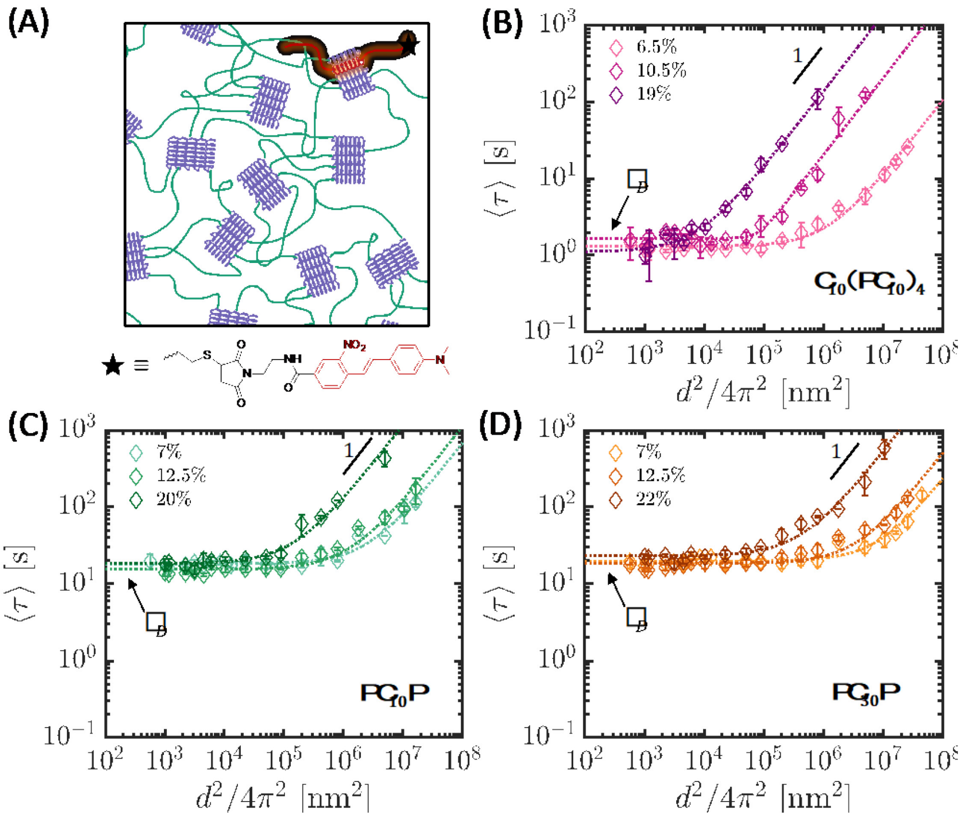

Figure 5. (A) Design of the tracer diffusion experiment of *o*-nitrostilbene-labeled C_5PC_5 molecules dispersed in the $PC_{10}P$, $PC_{30}P$, and $C_{10}(PC_{10})_4$ gels. (B-D) Forced Rayleigh scattering results of single-sticker tracer diffusion in each protein gel matrix at various concentrations, fit to the modified two-state model.

FRS results of single-sticker tracer diffusion through the protein gels are well-captured by the two-state model, as shown in **Figure 5**B-D. Unlike the multi-sticker proteins forming the network, the single-sticker tracer has exactly two well-defined association states (i.e., associated or free). Thus, the slow and fast diffusive modes from fits to the two-state model should correspond exactly to the associated and free states of the single-sticker tracer, and the parameters should reflect its intrinsic molecular diffusivity and association/dissociation kinetics. Tracer diffusion curves do not show a transition to a lower length scale Fickian regime as seen for the multi-sticker matrix proteins (see **Figure 3**), but instead exhibit a plateau in the relaxation time down to the smallest length scales. This small-length-scale plateau corresponds to a best-fit associated-state diffusivity of 0, i.e., $D_{slow} = 0$, which is consistent with previous tracer diffusion data of small-molecule stickers through metal-coordinate gels.[16] Because a single-sticker molecule cannot undergo diffusion by walking, this strongly implies minimal diffusive motion of the network junctions such that the single-sticker tracer is confined to a length scale smaller than the minimum d-spacing of the FRS measurement, i.e., $d_{tracer}/2\pi < 24$ nm, while in the associated state. This result is also consistent with the extent of junction fluctuations predicted by the phantom network model,[68] given the junction functionalities (i.e., 5 or 10) and strand lengths (i.e., root-mean-square end-to-end distance of 6.6 ± 0.5 for the C_{10} domain) of the protein gels here, and suggests that long-range diffusion of associated tracers within multi-chain aggregates is unlikely.

As shown by the two-state model,[16] the low-d^2 plateau in the tracer diffusion times is equal to the average dissociation time of the coiled-coil domain determined by the inverse of the dissociation rate, i.e., $\tau_D = k_D^{-1}$. That is, on small length scales, diffusion of the single-sticker tracer is controlled by the dissociation of the bound tracers, resulting in the diffusion timescale being independent of the length scale. As seen in **Figure 5**, the tracer dissociation times are roughly independent of concentration for each protein gel. In addition, the dissociation times are roughly equal for all telechelic PC_xP gels (with a range $\tau_D = 15 - 23$ s), whereas those for the four-sticker $C_{10}(PC_{10})_4$ gels are roughly 15-fold smaller ($\tau_D = 1.1 - 1.6$ s). As the coiled-coil domain in the single-sticker tracer is identical to the coiled-coil domains forming the network junctions, these dissociation times are expected to reflect the average dissociation times of all the network junctions in each gel.[16] Thus, while the dissociation times are roughly independent of the strand length (for the proteins studied here), they appear sensitive to the number of stickers per chain. This may arise from the difference in the junction functionality of the $C_{10}(PC_{10})_4$ gels compared to the telechelic gels (i.e., 10 vs 5, due to the strands flanking both sides of each coiled-coil domain in the four-sticker molecule), which may increase the dissociation rate through steric effects, or differences in the distribution of chain topologies (e.g., loops) between the different architectures. The tracer dissociation times are also comparable to the network relaxation times obtained from shear rheology for each gel (see **Figure 9** and Figure S12), consistent with previous observations that sticker dissociation is likely a pre-requisite step for network relaxation.[13,69]

The single-sticker characteristic timescales inferred from tracer diffusion measurements allow scaling estimates of the single-chain diffusive modes to be formulated as a comparison to the self-diffusion results. In a molecular walking step, a single coiled-coil sticker detaches with frequency k_D, after which the connecting strand is assumed to fully relax (thus exploring its pervaded volume, $V_{walk} \approx R_{C_x}^3$, where R_{C_x} is the root-mean-square end-to-end distance of the C_x strand) before the coiled-coil domain rebinds to a different network site. The single-chain walking diffusivity can thus be estimated as

$$D_{walk} \approx R_{C_x}^2 k_D \tag{8}$$

Note that this physical picture assumes a kinetics-limited system, such that conformational relaxation of the midblock strands is significantly faster than the sticker binding kinetics, which allows the chain to fully explore its pervaded volume before rebinding. This has been shown to be applicable to most associative networks studied experimentally,[13,16,29,70] including coiled-coil proteins such as those studied here.[15]

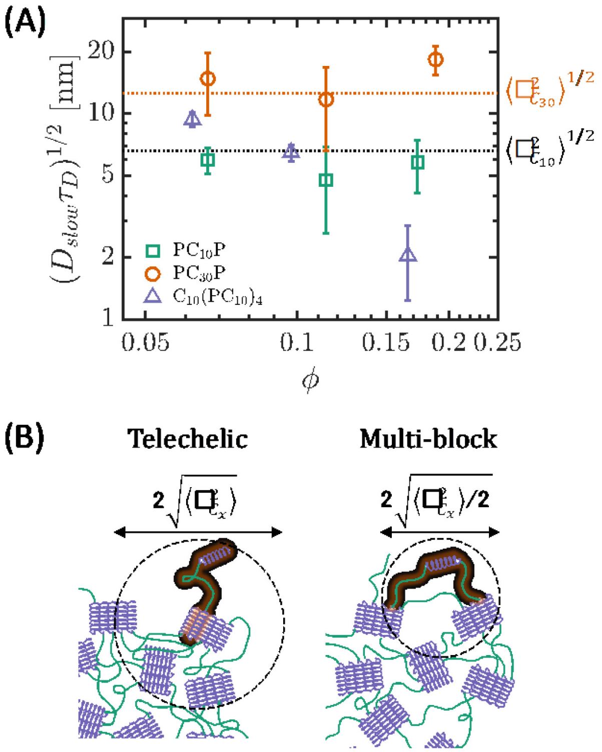

Figure 6. (A) Characteristic step size of the slow self-diffusive mode for all gels via $R_{slow} \approx (D_{slow}\tau_D)^{1/2}$. Horizontal lines indicate estimates for the unperturbed root-mean-square end-to-end distance of the C_{10} and C_{30} strands. (B) Schematic representations of the single-molecule walking step size for the telechelic PC_xP and multi-block $C_{10}(PC_{10})_4$ gels.

For all three proteins, the scaling estimate for D_{walk} is comparable to the values of D_{slow} from fits to the two-state model (see **Figure 3**), suggesting that single-chain walking gives rise to the slow mode in the associative protein gels. As a complementary perspective, empirical estimates for the characteristic step size of the slow mode can be obtained via $R_{slow} \approx (D_{slow}\tau_D)^{1/2}$, using the values of D_{slow} from fits to the two-state model. As shown in **Figure 6**A, for the telechelic PC_xP gels, the slow mode step size is similar to the unperturbed root-mean-square end-to-end distance of the midblock strands (either C_{10} or C_{30}) and displays no concentration dependence, consistent with a single-molecule walking mechanism on short length scales in the telechelic gels.

The slow mode step size for the four-sticker $C_{10}(PC_{10})_4$ gels is also on the same order as the C_{10} strand length, though it displays a strong decrease with concentration to below the C_{10} extension at the highest concentration. This qualitative difference in the concentration dependence between different molecular architectures may originate from the presence of two flanking strands for the middle two coiled-coil domains in the $C_{10}(PC_{10})_4$ protein, compared to only one for the telechelic proteins, which is predicted to decrease its walking step size by a factor of $\sqrt{2}$ as shown in **Figure 6**B.[26,68] Additional origins may include an increased tendency for a coiled-coil domain to re-associate to the same binding site in the $C_{10}(PC_{10})_4$ gels due to the limited chain mobility upon dissociation, which may increase the effective bond lifetime to beyond its intrinsic time τ_D. Similar arguments have been proposed as renormalization of the bond lifetime in the sticky Rouse theory,[18] which is expected to be enhanced in gels with more stickers per chain.

Comparing the timescale for the transition to the fast mode in self-diffusion measurements with the single-sticker dissociation rate is also consistent with the onset of single-molecule hopping with frequency k_{off}. The transition timescales normalized by the single-sticker dissociation time, τ_{off}/τ_D, are plotted for all gels in **Figure 7**A, where the interconversion timescales range from $10 - 1000$ times the coiled-coil dissociation time for these concentrations. For the telechelic PC_xP gels the transition times are roughly equal for all concentrations, around $\tau_{off}/\tau_D = 10$, whereas those for the four-sticker $C_{10}(PC_{10})_4$ gels increase noticeably with concentration, suggesting qualitative changes caused by the difference in the number of stickers per chain or other aspects of the molecular architecture.

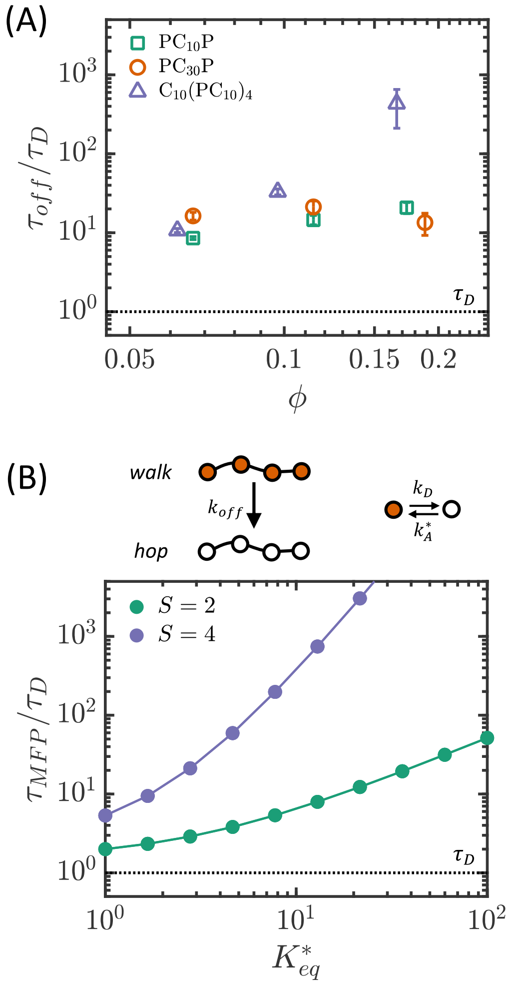

Figure 7. (A) Transition timescales from self-diffusion measurements normalized by the single-sticker dissociation time from tracer diffusion measurements for all protein gels. (B) Mean-first-passage time calculation of the single-molecule hopping frequency for chains with $S = 2$ and $S = 4$ stickers, starting from the fully bonded state (colored orange). Single-sticker association and dissociation are assumed to follow pseudo-first-order kinetics with rate constants $k_A^* = k_A F_{eq}$ and k_D, respectively. The pseudo-first-order equilibrium constant is defined as $K_{eq}^* = k_A^*/k_D^* = K_{eq}F_{eq}$ where F_{eq} is the equilibrium concentration of free binding sites in the gel.

To complement the experimental results, theoretical estimates for the frequency of single-molecule hopping can be obtained by solving for the mean-first-passage time for complete dissociation of a single chain with S stickers starting from the fully bonded state (see the SI for calculation details). Each sticker on the chain is assumed to undergo stochastic dissociation and association with pseudo-first-order rate constants k_D and k_A^*, respectively, which are specified as input parameters. Note that the dissociation rate directly determines the bond lifetime reflected by the single-sticker tracer dynamics, i.e., $\tau_D = k_D^{-1}$. Though the coiled-coil domains in the proteins assemble into pentamers, a pseudo-first-order association rate constant can be estimated from the true rate constant k_A and the equilibrium free binding site density F_{eq}, i.e., $k_A^* = k_A F_{eq}$. Similarly, a pseudo-first-order equilibrium constant for single-sticker association can be estimated via $K_{eq}^* = F_{eq} K_{eq}$, where $K_{eq} = k_A / k_D$ is the second-order equilibrium constant for coiled-coil association.[60] Note that the single-sticker equilibrium constants K_{eq} and K_{eq}^* are distinct from the two-state model parameter $\kappa_{eq} = k_{on} / k_{off}$ used earlier in Equation 6, which describes the interconversion between the two apparent self-diffusive species rather than individual stickers. As in previous work, the effective equilibrium constant of each sticker is assumed to be constant, independent of the number of stickers or association state of the chain, and the dynamics of each sticker are assumed to be uncorrelated.[26,27] Loops are also neglected, as they are unlikely to affect the hopping frequency due to the pentameric junction functionality of the gels here.

Normalized mean-first-passage times τ_{MFP} for interconversion from the fully bonded state to the fully unbonded state are similar in magnitude to the values of τ_{off} / τ_D seen experimentally, as shown in **Figure 7**B. The calculated mean-first-passage times depend on K_{eq}^* due to its effect on the association rate k_A^*, where a larger association rate increases the likelihood of reassociation of a released sticker before the remaining stickers can dissociate, increasing the chain dissociation time. Because the pseudo-first-order equilibrium constant is a function of concentration, the effect of increasing K_{eq}^{*} in the calculation can be interpreted as qualitatively analogous to increasing the total concentration ϕ experimentally. A clear difference in the scaling of τ_{MFP} with K_{eq}^{*} is observed between the 2-sticker and 4-sticker chains, with larger S increasing both the absolute value of τ_{MFP} and its concentration dependence qualitatively similar to experiment. This trend is broadly seen for the mean-first-passage dissociation times for all values of $S \in [2,6]$ (Figure S9).

The results of **Figure** 7A and **Figure** 7B are consistent with a self-diffusive transition to single-molecule hopping with an effective sticker equilibrium constant of $K_{eq}^{*} \approx 1-10$. These values are similar to coiled-coil binding equilibrium constants estimated in previous work,[42,60] which range between $K_{eq}^{*} = 10-20$, suggesting the validity of the single-molecule hopping mechanism. However, a quantitative match between the experimental and calculated interconversion times is not observed, which may result from a failure of the assumption of constant K_{eq}^{*} for each sticker. Recent work by Tirrell and coworkers has predicted a decrease in the effective equilibrium constant for binding of additional stickers on the same chain due to a loss of conformational entropy with each sticker attachment.[42] This effect may decrease the time required for complete dissociation of a chain, such that the experimental τ_{off} values may be lower than predicted by the mean-first-passage time calculation, particularly for chains with larger S. A decrease in the effective value of K_{eq}^{*} may cause the interconversion times for the four-sticker $C_{10}(PC_{10})_4$ gels to be closer to those of the two-sticker PC_xP gels than the mean-first-passage time predictions, as seen experimentally. However, without an independent estimate of the values of K_{eq}^{*} it is difficult to verify the entropic penalty predicted in Ref.[42] or its effect on the interconversion times seen in self-diffusion.

Effect of number of stickers on long-range diffusion. Comparing the terminal self-diffusion coefficients between proteins with different numbers of stickers further supports the single-chain hopping picture of long-range diffusion in associative networks. **Figure 8** displays the terminal effective diffusivity as a function of number of stickers per chain, comparing data from gels with constant junction density and strand length (i.e., with C_{10} strands). Data for $S = 1$ were taken from tracer diffusion measurements of C_5PC_5 through $PC_{10}P$ (7% and 12.5% w/v), data for $S = 2$ were taken from self-diffusion measurements of $PC_{10}P$ (7% and 12.5% w/v), and data for $S = 4$ were taken from self-diffusion measurements of $C_{10}(PC_{10})_4$ (10.5% and 19% w/v, such that the junction densities matched those of the $PC_{10}P$ gels). A linear correction was applied to the diffusion coefficients to account for differences in the molecular weight and gel concentration that may alter the fast diffusive mode, as done in prior work.[42] An analogous plot of the uncorrected diffusion coefficients is provided in Figure S13.

As expected, the terminal diffusion coefficients decrease both with total junction density and number of stickers per chain. For gels with the same junction density the corrected terminal diffusion coefficients appear to decrease roughly exponentially with the number of stickers per chain (albeit across a limited range of S). This can be compared to estimates for the terminal diffusion coefficient for a single-chain hopping mechanism[26,42] of $D_{hop} = p_0 D_{free}$, where D_{free} is the diffusivity of a free chain that is not associated to the network and p_0 is the equilibrium fraction of hopping chains. The fraction of hopping chains can be related to an *effective* single-sticker binding equilibrium constant K_{eff} via

$$D_{hop} = \frac{D_{free}}{1 + K_{eff}^{S}} \tag{9}$$

where the effective equilibrium constant can be related to the *intrinsic* equilibrium constants K_i for each sticker $i \in [1, S]$ on the chain, as shown by Tirrell and coworkers[42]:

$$K_{eff} = \left(K_1 + K_1 K_2 + \cdots + \prod_{i=1}^{S} K_i\right)^{\frac{1}{S}} \approx \left(\prod_{i=1}^{S} K_i\right)^{\frac{1}{S}} \tag{10}$$

where the last equality is valid for $K_i > 1$. Thus, for the general case of different sticker binding strengths, the effective single-sticker equilibrium constant is approximately the geometric average of the intrinsic single-sticker equilibrium constants. For constant K_i and D_{free} the terminal hopping diffusivity is expected to decay approximately exponentially with S as seen in Equation 9. Note that this is a significantly stronger dependence than the prediction of the sticky Rouse model,[18,19] which is a power-law $D_{eff} \sim S^{-2}$. However, if the sticker binding strength decreases with S due to an entropic penalty for binding,[42] this is also expected to yield a shallower-than-exponential scaling of D_{eff} with S due to the decrease in K_{eff} with S. The roughly exponential scaling seen in **Figure 8** for both junction densities is generally consistent with the prediction of Equation 9, suggesting a roughly constant K_{eff} with S for each junction density. The effective single-sticker equilibrium constants obtained from linear fits range between $K_{eff} = 1 - 10$, which are similar to the pseudo-first-order equilibrium constants K_{eq}^{*} estimated from the self-diffusion interconversion timescale (see **Figure 7**). Furthermore, extrapolation of the linear fits for each junction density to a chain with no stickers yields a constant value of $D_{eff}(S = 0) = 4 \times 10^5$ nm^2/s for both junction densities, which is similar to self-diffusivities reported for other macromolecules of similar molecular weight such as dextran and unbound globular proteins through hydrogels of similar concentrations.[71–73] Thus, the data suggest a relatively minor role of conformational entropy in modulating the effective single-sticker equilibrium constant and further support the role of single-chain hopping in controlling terminal self-diffusion of the protein gels. It should be noted that these observations are applicable for a relatively narrow range of $S \leq 4$, and that chains with more stickers may show a greater role of alternative diffusive modes such as long-range walking.[42]

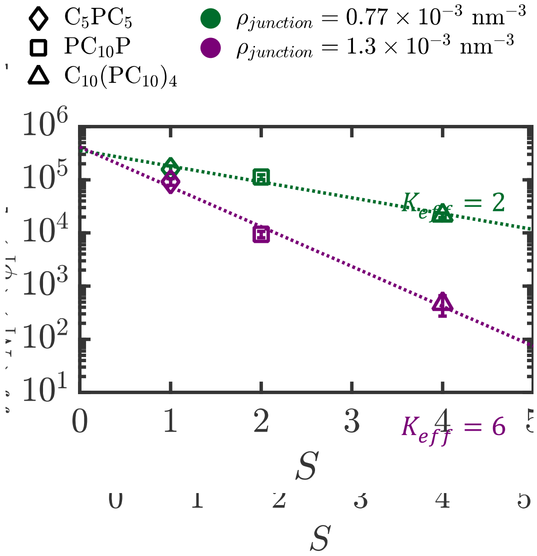

Figure 8. Terminal diffusivity, D_{eff}, of coiled-coil proteins as a function of number of stickers per chain, S, for gels with constant junction density, using linear corrections for differences in molecular weight and volume fraction.

Comparison of time scales. For all gels, the single-sticker dissociation time τ_D (from tracer diffusion experiments) is smaller than the interconversion timescale τ_{off} from self-diffusion experiments, consistent with the need for multiple bonds to dissociate to initiate a single-molecule hopping event that ultimately leads to terminal diffusion. In **Figure 9** these relaxation times are examined in relation to frequency sweep data of the same gels at 35 °C, again comparing gels with equal junction densities. All gels exhibit a high-frequency plateau modulus, G_p, and a mid-frequency crossover between storage and loss moduli, allowing the macroscopic network relaxation time to be identified via $\tau_{ex} = \omega_c^{-1}$. These quantities are used to normalize the dynamic moduli and frequencies, respectively, resulting in satisfactory alignment of the frequency sweeps of all gels suggesting self-similar relaxation behavior (though the terminal region is not fully developed for the telechelic PC$_x$P gels within the measurement range).

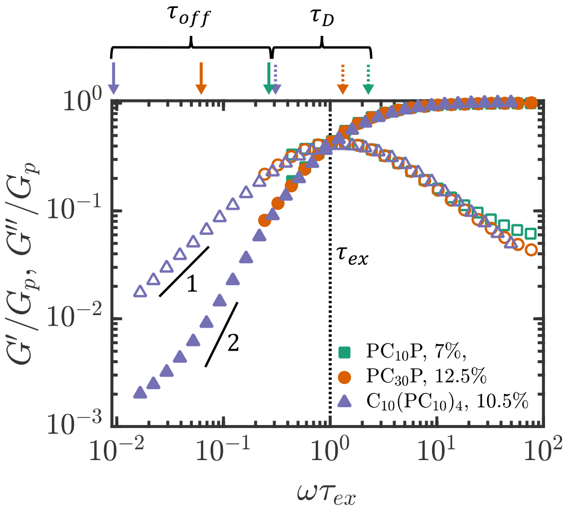

Figure 9. Reduced frequency sweeps of PC$_{10}$P (7% w/v), PC$_{30}$P (12.5% w/v), and C$_{10}$(PC$_{10}$)$_4$ (10.5% w/v) at 35 °C, where the dynamic moduli are normalized by the high-frequency plateau elastic modulus G_p and the frequencies are normalized by the relaxation time defined by the crossover frequency $\tau_{ex} = \omega_c^{-1}$. All gels have the same junction density $\rho_{junction} = 0.77 \times 10^{-3}$ nm^3. Filled symbols and unfilled symbols indicate storage and loss moduli, respectively. Characteristic timescales τ_D and τ_{off} are indicated by arrows for each gel.

The single-sticker dissociation times τ_D are within an order of magnitude of the network relaxation time τ_{ex}, consistent with sticker dissociation being a limiting step in network relaxation. This similarity between the sticker dissociation and network relaxation time scales has previously been observed and suggests that single bond dissociation events are sufficient to enable stress relaxation through junction exchange.[13,16,17,38] In contrast, the self-diffusion interconversion times

τ_{off} are $10 - 100$ times greater than $\tau_{ex} \approx \tau_D$, with no conclusive rheological signature for this relaxation process yet identified.[17,65] The results provide further evidence that self-diffusion and network relaxation are governed by fundamentally different processes, where network relaxation requires exchange of only single stickers on the time scale $\sim\tau_D$ while long-range self-diffusion requires a longer relaxation time $\sim\tau_{off}$ governed by the dissociation of all stickers on a molecule to begin a hopping event.

CONCLUSIONS

In this work, the combination of structural and self-diffusion measurements on model associative protein hydrogels provides a molecular picture of chain dynamics in associative networks, suggesting the validity of single-chain models with only a minor effect of multi-chain correlations or network heterogeneity on long time scales. Structural characterization by neutron scattering and fluorescence microscopy provides evidence for a large-scale correlation length $\sim 1 - 5$ times the mean inter-junction spacing, suggesting mild inhomogeneity in the junction and chain distribution, but no macroscopic clustering or phase separation. Self-diffusion measurements reveal a transition between slow and fast diffusive modes in all gels on length scales similar to the multi-chain correlation length. Comparison to the single-sticker dissociation time suggests that single-chain mechanisms are sufficient to describe self-diffusion across a range of length scales as conceptualized in previous studies. The step size of the slow diffusive mode is commensurate with the end-to-end distance of the bridging strands, suggesting a single-chain walking mode rather than collective motion of multi-chain aggregates. In addition, the transition to the fast mode occurs on time scales consistent with the dissociation of all the stickers on a chain as estimated from mean-first-passage-time calculations, suggesting the onset of single-molecule hopping. Finally, the terminal diffusivity is found to follow an exponential dependence on the number of stickers per chain, which is consistent with large-scale diffusion occurring by molecular hopping rather than sticky Rouse motion. These results support single-chain models of associative polymer dynamics previously proposed and may be generalizable to other associative systems with different sticker chemistry and chain architectures.

ASSOCIATED CONTENT

The Supplementary Information is available at [link inserted by publisher]

AUTHOR INFORMATION

Corresponding Author

*(B.D.O) Email bdolsen@mit.edu

Notes

The authors declare no competing financial interest.

ACKNOWLEDGMENT

This work was supported by the National Science Foundation under Award DMR-1709315. A.R. acknowledges support from the Department of Defense through a National Defense Science and Engineering Graduate Fellowship. The authors acknowledge Danielle J. Mai for assistance with protein synthesis, Wei-Ren Chen for assistance with ultra-small-angle neutron scattering measurements, and Changwoo Do, Carrie Gao, and William Heller for assistance with small-angle neutron scattering measurements.

REFERENCES

1 S. Seiffert and J. Sprakel, *Chem. Soc. Rev.*, 2012, **41**, 909–930.

2 S. L. Craig and D. Xu, *Langmuir*, 2007, **23**, 1626–1634.

3 E. A. Appel, J. Del Barrio, X. J. Loh and O. A. Scherman, *Chem. Soc. Rev.*, 2012, **41**, 6195–6214.

4 J. Teßmar, F. Brandl and A. Göpferich, *Fundam. Tissue Eng. Regen. Med.*, 2009, **101**, 495–517.

5 M. J. Webber, E. A. Appel, E. W. Meijer and R. Langer, *Nat. Mater.*, 2015, **15**, 13–26.

6 C. H. Li, C. Wang, C. Keplinger, J. L. Zuo, L. Jin, Y. Sun, P. Zheng, Y. Cao, F. Lissel, C. Linder, X. Z. You and Z. Bao, *Nat. Chem.*, 2016, **8**, 618–624.

7 B. C. K. Tee, C. Wang, R. Allen and Z. Bao, *Nat. Nanotechnol.*, 2012, **7**, 825–832.

8 K. E. Feldman, M. J. Kade, E. W. Meijer, C. J. Hawker and E. J. Kramer, *Macromolecules*, 2009, **42**, 9072–9081.

9 C. L. Lewis, K. Stewart and M. Anthamatten, *Macromolecules*, 2014, **47**, 729–740.

10 J. C. Olivia R. Cromwell and and Z. Guan, *J Am Chem Soc*, 2009, **48**, 35–56.

11 R. S. Hoy and G. H. Fredrickson, *J. Chem. Phys.*, 2009, **131**, 224902.

12 E. B. Stukalin, L. H. Cai, N. A. Kumar, L. Leibler and M. Rubinstein, *Macromolecules*, 2013, **46**, 7525–7541.

13 W. C. Yount, D. M. Loveless and S. L. Craig, *J. Am. Chem. Soc.*, 2005, **127**, 14488–14496.

14 N. Holten-Andersen, M. J. Harrington, H. Birkedal, B. P. Lee, P. B. Messersmith, K. Y. C. Lee and J. H. Waite, *Proc. Natl. Acad. Sci.*, 2011, **108**, 2651–2655.

15 A. Rao, H. Yao and B. D. Olsen, *Phys. Rev. Res.*, 2020, **2**, 043369.

16 S. Tang and B. D. Olsen, *Macromolecules*, 2016, **49**, 9163–9175.

17 S. Tang, M. Wang and B. D. Olsen, *J. Am. Chem. Soc.*, 2015, **137**, 3946–3957.

18 M. Rubinstein and A. N. Semenov, *Macromolecules*, 1998, 31, 1386–1397.

19 L. G. Baxandall, *Macromolecules*, 1989, **22**, 1982–1988.

20 F. Tanaka and S. F. Edwards, *J. Nonnewton. Fluid Mech.*, 1992, **43**, 289–309.

21 T. Annable, R. Buscall, R. Ettelaie and D. Whittlestone, *J. Rheol. (N. Y. N. Y).*, 1993, **37**, 695–726.

22 F. Tanaka and S. F. Edwards, *Macromolecules*, 1992, **25**, 1516–1523.

23 M. K. Sing, Z. G. Wang, G. H. McKinley and B. D. Olsen, *Soft Matter*, 2015, **11**, 2085–2096.

24 A. N. Semenov and M. Rubinstein, *Macromolecules*, 1998, **31**, 1373–1385.

25 M. Rubinstein and A. N. Semenov, *Macromolecules*, 2001, **34**, 1058–1068.

26 J. Ramirez, T. J. Dursch and B. D. Olsen, *Macromolecules*, 2018, **51**, 2517–2525.

27 A. Rao, J. Ramírez and B. D. Olsen, *Macromolecules*, 2021, **54**, 11212–11227.

28 I. Mahmad Rasid, N. Holten-Andersen and B. D. Olsen, *Macromolecules*, 2021, **54**, 1354–1365.

29 S. Tang, A. Habicht, S. Li, S. Seiffert and B. D. Olsen, *Macromolecules*, 2016, **49**, 5599–5608.

30 S. Seiffert, *Prog. Polym. Sci.*, 2017, **66**, 1–21.

31 S. Seiffert, *Polym. Chem.*, 2017, **8**, 4472–4487.

32 M. Shibayama, *Bull. Chem. Soc. Jpn.*, 2006, **79**, 1799–1819.

33 S. Koizumi, M. Monkenbusch, D. Richter, D. Schwahn and B. Farago, *J. Chem. Phys.*, 2004, **121**, 12721–12731.

34 M. Shibayama, T. Tanaka and C. C. Han, *J. Chem. Phys.*, 1992, **97**, 6829–6841.

35 M. Zhong, R. Wang, K. Kawamoto, B. D. Olsen and J. A. Johnson, *Science (80-.).*, 2016, **353**, 1264–1268.

36 H. Zhou, J. Woo, A. M. Cok, M. Wang, B. D. Olsen and J. A. Johnson, *Proc. Natl. Acad. Sci. U. S. A.*, 2012, **109**, 19119–19124.

37 M. J. Glassman, J. Chan and B. D. Olsen, *Adv. Funct. Mater.*, 2013, **23**, 1182–1193.

38 I. Mahmad Rasid, C. Do, N. Holten-Andersen and B. D. Olsen, *Soft Matter*, 2021, **17**, 8960–8972.

39 F. Ikkai and M. Shibayama, *Phys. Rev. Lett.*, 1999, **82**, 4946–4949.

40 M. Shibayama, M. Tsujimoto and F. Ikkai, *Macromolecules*, 2000, **33**, 7868–7876.

41 A. Jangezehi, R. Ghaffarian, W. Schmolke and S. Seiffert, *Macromolecules*, 2018, **51**, 2859–2871.

42 P. B. Rapp, A. K. Omar, B. R. Silverman, Z.-G. Wang and D. A. Tirrell, *J. Am. Chem. Soc.*, 2018, **140**, 14185–14194.

43 A. K. Omar and Z. G. Wang, *Phys. Rev. Lett.*, 2017, **119**, 1–5.

44 B. D. Olsen, J. A. Kornfield and D. A. Tirrell, *Macromolecules*, 2010, **43**, 9094–9099.

45 W. Shen, K. Zhang, J. A. Kornfield and D. A. Tirrell, *Nat. Mater.*, 2006, **5**, 153–158.

46 W. A. Petka, J. L. Harde, K. P. McGrath, D. Wirtz, D. A. Tirrell, J. L. Harden, K. P. McGrath, D. Wirtz and D. A. Tirrell, *Science (80-.).*, 1998, **281**, 389–392.

47 M. Shibayama, *Macromol. Chem. Phys.*, 1998, **199**, 1–30.

48 M. Wang, K. Timachova and B. D. Olsen, *Macromolecules*, 2013, **46**, 1651–1658.

49 W. T. Heller, J. Hetrick, J. Bilheux, J. M. B. Calvo, W.-R. Chen, L. DeBeer-Schmitt, C. Do, M. Doucet, M. R. Fitzsimmons, W. F. Godoy, G. E. Granroth, S. Hahn, L. He, F. Islam, J. Lin, K. C. Littrell, M. McDonnell, J. McGaha, P. F. Peterson, S. V. Pingali, S. Qian, A. T. Savici, Y. Shang, C. B. Stanley, V. S. Urban, R. E. Whitfield, C. Zhang, W. Zhou, J. J. Billings, M. J. Cuneo, R. M. F. Leal, T. Wang and B. Wu, *SoftwareX*, 2022, **19**, 101101.

50 M. Agamalian, L. Heroux, K. C. Littrell and J. M. Carpenter, *J. Phys. Conf. Ser.*, 2018, **1021**, 2–7.

51 W. T. Heller, M. Cuneo, L. Debeer-Schmitt, C. Do, L. He, L. Heroux, K. Littrell, S. V. Pingali, S. Qian, C. Stanley, V. S. Urban, B. Wu and W. Bras, *J. Appl. Crystallogr.*, 2018, **51**, 242–248.

52 D. Ehlich and H. Sillescu, *Macromolecules*, 1990, 23, 1600–1610.

53 V. N. Malashkevich, R. A. Kammerer, V. P. Efimov, T. Schulthess and J. Engel, *Science (80-.).*, 1996, **274**, 761–765.

54 W. Shen, J. A. Kornfield and D. A. Tirrell, *Soft Matter*, 2007, **3**, 99–107.

55 C. E. R. Edwards, D. J. Mai, S. Tang and B. D. Olsen, *Phys. Rev. Mater.*, 2020, **4**, 35–37.

56 A. M. Hecht, F. Horkay, P. Schleger and E. Geissler, *Macromolecules*, 2002, **35**, 8552–8555.

57 S. Mallam, F. Horkay, A. M. Hecht, A. R. Rennie and E. Geissler, *Macromolecules*, 1991, **24**, 543–548.

58 F. Horkay, A. M. Hecht, S. Mallam, E. Geissler and A. R. Rennie, *Macromolecules*, 1991, **24**, 2896–2902.

59 P. G. De Gennes, *Scaling Concepts in Polymer Physics*, Cornell University Press, 1979.

60 P. B. Rapp, A. K. Omar, J. J. Shen, M. E. Buck, Z. G. Wang and D. A. Tirrell, *J. Am. Chem. Soc.*, 2017, **139**, 3796–3804.

61 R. Wang, A. Alexander-Katz, J. A. Johnson and B. D. Olsen, *Phys. Rev. Lett.*, 2016, **116**, 1–5.

62 P. N. Pusey and W. Van Megan, *Physica A*, 1989, **157**, 705–741.

63 J. G. H. Joosten, J. L. McCarthy and P. N. Pusey, *Macromolecules*, 1991, 24, 6690–6699.

64 T. Kanaya, N. Takahashi, K. Nishida, H. Seto, M. Nagao and T. Takeda, *Phys. Rev. E - Stat. Nonlinear, Soft Matter Phys.*, 2005, **71**, 1–7.

65 I. Mahmad Rasid, A. Rao, N. Holten-Andersen and B. D. Olsen, *Macromolecules*, 2022, **55**, 6056–6066.

66 S. Maccarrone, C. Scherzinger, O. Holderer, P. Lindner, M. Sharp, W. Richtering and D. Richter, *Macromolecules*, 2014, **47**, 5982–5988.

67 A. Ghavami, H. Kobayashi and R. G. Winkler, *J. Chem. Phys.*, 2016, **145**, 1–10.

68 H. M. James, *J. Chem. Phys.*, 1947, **15**, 651–668.

69 W. Shen, J. A. Kornfield and D. A. Tirrell, *Macromolecules*, 2007, **40**, 689–692.

70 T. Rossow, A. Habicht and S. Seiffert, *Macromolecules*, 2014, 47, 6473–6482.

71 K. Engberg and C. W. Frank, *Biomed. Mater.*, , DOI:10.1088/1748-6041/6/5/055006.

72 G. M. Cruise, D. S. Scharp and J. A. Hubbell, *Biomaterials*, 1998, **19**, 1287–1294.

73 S. Pajević, R. Bansil and Č. Koňák, *Macromolecules*, 1993, **26**, 305–312.